Erschienen in: Faraday Discussions ; 235 (2022). - S. 132-147
https://dx.doi.org/10.1039/D1FD00087J

Influence of anisotropy on heterogeneous nucleation of gold nanorod assemblies

Ann-Kathrin Göppert, Guillermo González-Rubio and Helmut Cölfen *

In this study, we analysed for the first time heterogeneous nucleation with anisotropic nanoparticles as a model system for non-spherical building units on the nanoscale. Gold nanorods were synthesised and assembled to investigate the phenomenon of heterogeneous nucleation. To determine the influence of the particle shape on heterogeneous nucleation, we utilised gold nanorods with varying aspect ratios, ranging from 3.00 and 2.25 to 1.75, while keeping the surface chemistry constant. First, the nucleation of the gold nanorod assemblies in solution and the process kinetics were analyzed with UV-vis-NIR spectroscopy followed by a microscopic examination of the gold nanorod-based superstructures formed heterogeneously on substrates. Here, positively charged cetyltrimethylammonium bromide (CTAB)-functionalized gold nanorods and negatively charged polystyrene sulfonate (PSS) functionalized substrates ensured the directed heterogeneous nucleation on the substrates. A combination of light microscopy with simultaneous UV-vis-NIR spectroscopy allowed us to observe the gold nanorod-based superstructure formation on the substrates *in situ* and to determine the nucleation rates of the process. We analysed the resulting data with the classical nucleation theory, which revealed a dominating kinetic term and a negligible thermodynamic term in contrast to ionic systems like calcium carbonate. Our studies consistently exhibit an influence of the aspect ratio on the nucleation behaviour resulting in faster nucleation of superstructures as the aspect ratio decreases. Hence our studies show unprecedented insight into the influence of particle anisotropy on the nucleation and growth of nanorod-based superstructures and reveal significant differences in the nucleation of nanoparticle building units compared to the nucleation of atoms or molecules as building units.

Introduction

Heterogeneous nucleation is a common phenomenon in nature, evident for example, in the formation of clouds or biominerals.[1,2] However, it is no less

Physikalische Chemie, Universität Konstanz, Universitätsstr. 10, D-78457 Konstanz, Germany. E-mail: helmut.coelfen@uni-konstanz.de

important in industrial applications, like the hardening of cement or the formation of mineral scale in pipes.[3,4] Despite its relevance, heterogeneous nucleation is not fully understood, probably due to the demanding analysis required to investigate it, which entails high spatial and temporal resolution at the same time.[5,6] To simplify the analysis of nucleation phenomena, micron-sized particles have been proposed and exploited as model systems for atoms or molecules building up to bigger superstructures.[7–10] Most analysed microparticle-based systems rely on isotropic hard spheres as the simplest system for nucleation. Today, we have a relatively good understanding of the nucleation of hard spherical particles into superstructures thanks to the use of a combination of computer simulations[11,12] and experiments utilizing, for example, spherical PMMA particles.[13–18]

Although most work on nucleation and crystallization focuses on isotropic particles as building units, systems with anisotropic particles or building units are of great importance to investigate many crystallization phenomena. For example, in concrete where nucleation of the anisotropic calcium silicate hydrate platelets to superstructures leads to hardening of the material.[19,20] Concrete is the second most widely used material on earth, and its vast carbon dioxide emission urges us to adapt greener alternatives like magnesium silicates.[21] An understanding and manipulation of the nucleation process in these anisotropic systems can thus potentially help to improve the properties of magnesium silicate-based or alternative concrete, allowing a partial replacement of calcium silicates. Proteins constitute another prominent example, as they can also exhibit anisotropic forms. Today, X-ray crystallography remains the gold standard for the determination of the macromolecular structure of proteins.[22] However, the crystallization of proteins, which is needed for analysis with X-ray crystallography, is extremely challenging. Also, in this example, a better understanding of the nucleation of anisotropic proteins can bring us to a more controlled crystallization of proteins and thus simplify their analysis enormously.

Moreover, anisotropic nanoparticles have direction-dependent properties like different shapes or surface chemistry. *Via* the shape of a particle, the properties of the single-particle such as electronic,[23] catalytic,[24] or magnetic,[25,26] can be influenced.[27] Beyond that, anisotropic particles can not only assemble to simple closest packing, like isotropic spherical particles, but furthermore, they can assemble into more complex structures.[28–31] Here, the nature of the resulting bulk material depends on the nanoparticle-based superstructure and determines its macroscopic properties. This is the field of non-classical crystallization, with mesocrystals as a prominent example.[28,32–34] Therefore, anisotropic building units from molecules to particles are not only common in nature but additionally open the possibility to design new material properties resulting from a variation in the assembly structures.[35] However, in many cases, it is yet unclear how the shape of the building units influences the nucleation events that eventually lead to the formation of nanoparticle-based materials.

In this study, we focused on investigating the phenomenon of heterogeneous nucleation with anisotropic particles as building units on the nanoscale. Nanoparticles show more similar behaviour to atoms and molecules than microparticles due to their similar dimensions and diffusion properties, and are therefore well suited as model systems. There are already a lot of examples for the (heterogeneous) nucleation of nanoparticles on substrates, which play an

important role for the formation and analysis of nanoparticle assemblies. Typical subsequent characterizations of nanoparticle assemblies like transmission electron microscopy (TEM), scanning electron microscopy (SEM), atomic force microscopy (AFM), or small-angle X-ray scattering (SAXS) require the immobilization of the nanoparticle superstructures on a substrate. In retrospect, it can be difficult to estimate whether the superstructures nucleated heterogeneously on the substrate, if the substrate had any influence on the structures formed, or how big this influence was.[35] Here, theoretical investigations can be helpful, like the example of Luedtke *et al.* who simulated dodecanethiol capped gold nanoparticles adsorbing on the basal plane of graphite.[36] The simulations of the hydrocarbon chains while attaching to the substrate and with this an edge orientation of the nanoparticles further induced the resulting structure of the superstructures. Next to planar substrates textured substrates on the order of the nanoparticle diameter open the possibility of direct structural control during nucleation and growth. For instance, lithographically patterned templates can trap solvated nanoparticles over capillary forces,[37–39] or periodically structured templates allow the arrangement of gold nanorods to plasmonic supercrystals.[40] Further, spherical substrates like emulsion droplets[41] or microspheres[42] can be used to control the structuring of nanoparticle assemblies. Additionally, the assembly of cadmium selenide nanoparticles to monolayers at liquid–liquid interfaces give more insight into the formation mechanism.[43] Pendant drop tensiometry and *ex situ* TEM measurements showed three steps in this process: first free nanoparticle diffusion to the interface, second, a closer packing of the nanoparticles to clusters, and third, a thermally activated exchange between incoming and adsorbed nanoparticles resulting in a dense packed monolayer. Another example at liquid–liquid interfaces constitutes the assembly of tri-*n*-octylphosphine oxide-covered cadmium selenide nanorods.[44] The structure of these assemblies ranged from low density smectic packing over more dense columnar ordering to crystalline-like phases. These different structures could be induced by varying the interfacial energy between the liquids and the nanorods, the concentration of the nanorods, or the aspect ratio of the nanorods.

To gain better insight into how the shape of the building units or more precisely the particle anisotropy, influences the heterogeneous nucleation of nanoparticles into superstructures, we utilised gold nanorods with similar width and distinct aspect ratios while keeping their surface chemistry constant. First, the nucleation of the gold nanorod assemblies in solution was analysed followed by an examination of the gold nanorod superstructures formed heterogeneously on substrates. A combination of light microscopy with simultaneous UV-vis-NIR (ultraviolet-visible-near-infrared) spectroscopy allowed us to observe the gold nanorod-based superstructure formation on the substrates *in situ* and determine the nucleation rates of this process.

Results and discussion

Gold nanorods

Our project aimed to analyse the impact of nanoparticle anisotropy on heterogeneous nucleation into superstructures. Therefore, gold nanorods were chosen as building blocks due to their ease of synthesis, low size dispersity, tuneable anisotropy, and ability to self-assemble into (meso)crystalline superstructures.

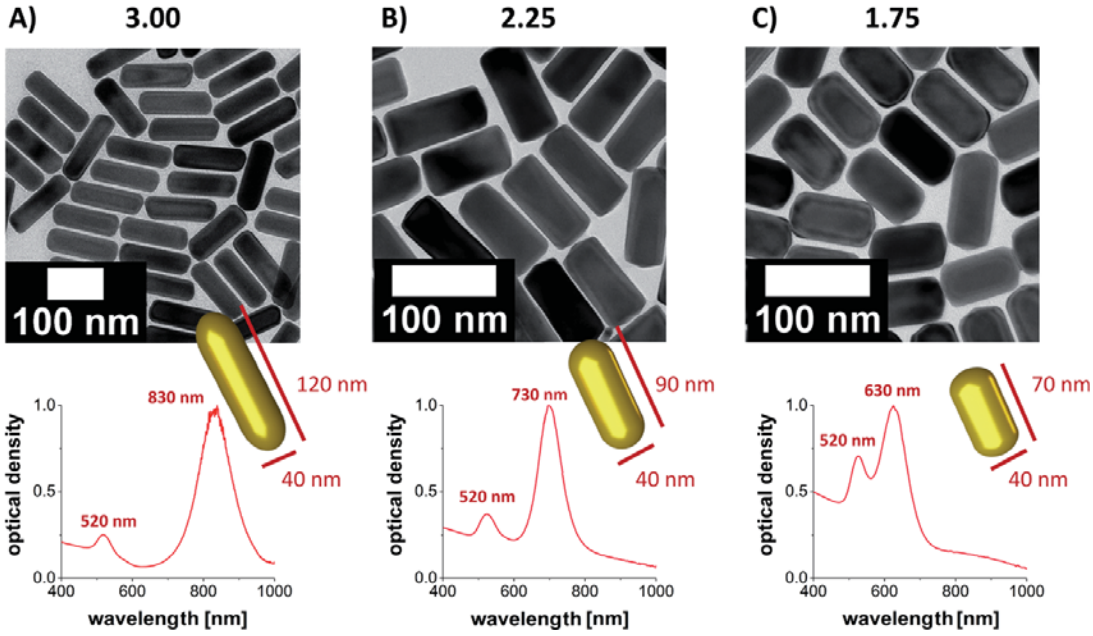

Fig. 1 Gold nanorods with various aspect ratios utilised in the heterogeneous nucleation experiments. The upper row shows HR-TEM images of the gold nanorods with aspect ratios of (A) 3.00, (B) 2.25, and (C) 1.75 and the bottom row shows the corresponding UV-vis-NIR spectra and a scheme with the edge lengths of the gold nanorods.

Moreover, their strong plasmonic activity, which is sensitive to the nanoparticle aggregation state, enables the use of UV-vis-NIR spectroscopy to investigate self-assembly and nucleation processes. The synthesis of colloidal gold nanoparticles with controlled dimensions and low size dispersity can typically be achieved by seed-mediated growth methods based on the spatial and temporal separation of nucleation and growth stages.[45,46] More specifically, in this work, we synthesised three gold nanorod samples with a different aspect ratio (detailed description in the experimental part).[47] Thereby, gold nanorods of 40 nm in diameter and lengths of 120, 90, and 70 nm, corresponding to aspect ratios of 3.00, 2.25, and 1.75, respectively, were successfully prepared. The resulting nanorods presented narrow plasmon bands of 830, 730 and 630 nm (Fig. 1).

Controlled nucleation in solution

The system of three identical gold nanorods only varying in their aspect ratio allowed the study of the influence of the particle shape on the heterogeneous nucleation of these gold nanorods into superstructures. To investigate the heterogeneous nucleation experiments in a reproducible manner, a methodology for the controlled destabilization of the gold nanorod dispersions was first required. This type of colloidal gold nanocrystal is stabilised through the adsorption of cationic cetyltrimethylammonium bromide (CTAB) micelles on their surface, which is the surfactant utilised during their synthesis as a stabilizing and shape directing agent. When aiming at the controlled self-assembly of the gold nanorods, destabilisation of such electrostatic forces through the addition of water-soluble organic solvents probably represents the most straightforward strategy.[35,48,49] In our case, we choose ethanol to trigger the gold nanorod self-assembly into superstructures. Then, to obtain information about the

aggregation process, we employed UV-vis-NIR spectroscopy, as it is proven to be a helpful analytic in the case of plasmonic gold nanoparticles where their optical properties are sensitive to the presence of other plasmonic particles in the vicinity.[50] This fact opens access to characterise the self-assembly process *via* UV-vis-NIR spectroscopy directly in solution and receives fast insight into the destabilization process (ESI Fig. S1†).[51,52] The gold nanorods present two characteristic plasmonic bands: a transversal resonance mode located at approximately 530 nm, and a longitudinal mode at longer wavelengths that depends on the aspect ratio.[53] During the nucleation and self-assembly process, a shift and broadening of the longitudinal plasmon bands for all investigated nanorod colloids were observed, meaning new bands corresponding to the formation of aggregates emerged at longer wavelengths.[50,54,55] Overall, these results indicate the suitability of using ethanol to trigger the aggregation of CTAB-stabilised gold nanorods. Moreover, analysis of the destabilization kinetics showed that the reactions proceeded as a second-order reaction (ESI Table S1†). These findings suggest a mechanism based on bimolecular collisions.

Heterogeneous nucleation on substrates

After a methodology for the controlled destabilization of gold nanorods was established, in the next step, we aimed to accomplish heterogeneous nucleation and growth of the gold nanorod-based superstructures triggered by solid substrates. The utilization of CTAB as a colloidal stabilizing agent results in gold nanorods with a positively charged surface due to the quaternary ammonium cation of CTAB. To ensure a favourable interaction of the positively charged gold nanorods with the desired substrate, we functionalized the surface of mica substrates with negatively charged polystyrene sulfonate (detailed description in the experimental part). In addition, the use of mica substrates, which are atomically cleavable and thereby exhibit a very smooth surface, allows us to minimize the potential undesired nucleation triggered by cracks or the roughness on the surface. The interaction of the gold nanorods with the sulfonate-functionalized mica substrates was evaluated by destabilizing gold nanorods in the presence of these substrates *via* UV-vis-NIR spectroscopy. The self-assembly kinetics were then compared with that of samples destabilized in the absence of substrates (ESI Fig. S2†). The experiments showed that sulfonate-functionalized substrates can successfully enhance the destabilisation of the gold nanorod dispersions. Consistent with this finding, we obtained similar results with a favourable interaction for CTAB stabilized gold nanocubes with sulfonate-functionalized substrates in another project.[56]

In the next step, we examined if the sulfonate-functionalized substrates can effectively lead to a superstructure growth on their surface *via* scanning electron microscopy (SEM) (Fig. 2). Here, the rods form randomly organized assemblies which is not surprising given the short building time of 40 min. The rods with an aspect ratio of 3.00 formed large superstructures up to a size of around 5 μm, which tend to be elongated and tattered. However, lower aspect ratios (2.25 and 1.75) lead to more and denser-packed gold nanorod superstructures with larger dimensions of up to 10 μm for the aspect ratio of 1.75 (ESI Table S2 and Fig. S3†). Overall, these results show that sulfonate-functionalized substrates not only enhanced the destabilization of the gold nanorods but further led to the heterogeneous nucleation and growth of gold nanorod-based superstructures on

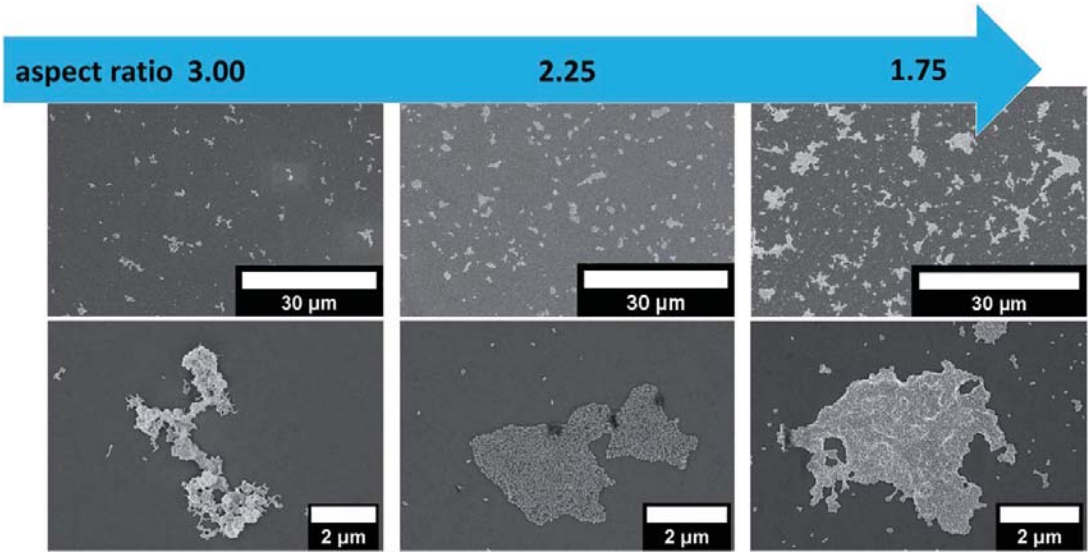

Fig. 2 Gold nanorod-based superstructures. SEM images of gold nanorod-based superstructures on sulfonate-functionalised substrates. The gold nanorods have various aspect ratios: 3.00 (left column), 2.25 (middle column), and 1.75 (right column). The density of superstructures on the substrate is less for gold nanorods with a high aspect ratio (3.00) and the superstructures seem to be more tattered. Going to lower aspect ratios (1.75), the density of superstructures increases, the superstructures seem to become more compact, and increase in height.

the substrate surface. Thus, the combination with sulfonate-functionalized substrates was chosen for the heterogeneous nucleation experiments.

Analysing heterogeneous nucleation kinetics

The heterogeneous nucleation of the gold nanorod-based superstructures on sulfonate-functionalised mica substrates was analysed with light microscopy and simultaneous UV-vis-NIR spectroscopy. We explained this general approach in detail in a previous publication and refer the reader to more detailed information about the experimental set-up and the evaluation of the data in that publication.[56] For this project, a hydrophobised quartz cuvette was used as a vessel for the heterogeneous nucleation experiments. The gold nanorods came into contact with the sulfonate-functionalised mica substrates through a hole in the cuvette. With light microscopy, it was possible to observe the superstructure growth on the mica surface, which opened the possibility to analyse the kinetics of the heterogeneous nucleation. The simultaneous UV-vis-NIR measurement gave information about the gold nanorod concentration and potential undesired homogeneous nucleation processes. The gold nanorods were then destabilized in a controlled manner with 20 vol% ethanol to ensure the colloidal stability of the nanoparticles in solution while enabling the superstructure growth on the substrate (ESI Fig. S4†). A detailed comparison of the results obtained from the different investigated nanorod aspect ratios (Fig. 3) showed that the number of superstructures detected on the substrate *via* light microscopy, their formation speed and with it the slope, correlate with their anisotropy degree. For instance, gold nanorods with a high aspect ratio (3.00) tended to form fewer superstructures and exhibited lower nucleation rates. However, those gold nanorods with

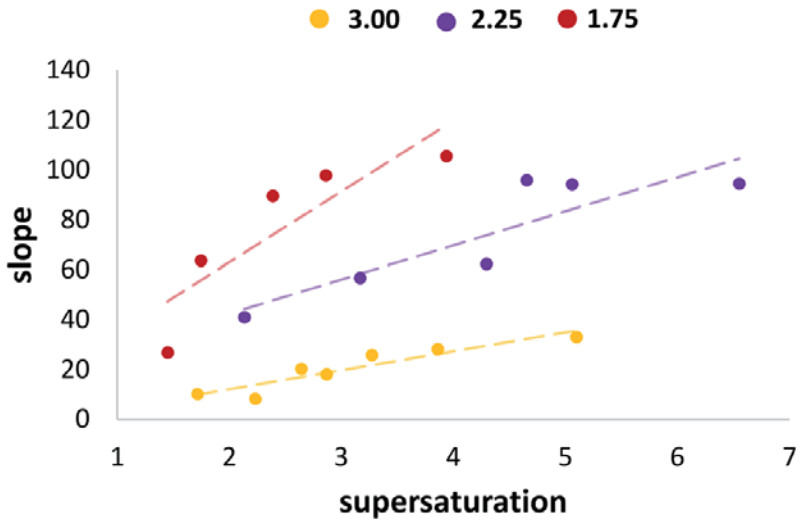

Fig. 3 Slopes of superstructure growth dependent on the aspect ratio. The determined slopes are the number of counted superstructures against the experiment time, which is equivalent to the nonnormalized nucleation rate. These slopes are plotted against the supersaturation for gold nanorods with varying aspect ratios: 3.00 (yellow), 2.25 (purple), and 1.75 (red).

a lower aspect ratio (1.75) nucleated faster and formed a higher number of superstructures. These findings are consistent with the results obtained from SEM characterisation experiments (Fig. 2) where gold nanorods with a lower anisotropy degree (1.75) formed more, denser-packed and bigger superstructures.

A logarithmic plot of the nucleation rates J_n against the inverse square of the supersaturations σ (Fig. 4) allowed us to determine the interfacial energies α for the heterogeneous nucleation process according to eqn (1).[5]

$$\ln(J_n) = -\frac{f\Omega^2}{(k_B T)^3}\alpha^3\left(\frac{1}{\sigma^2}\right) + \ln\left(A \times e^{-\frac{E_A}{k_B T}}\right) \quad (1)$$

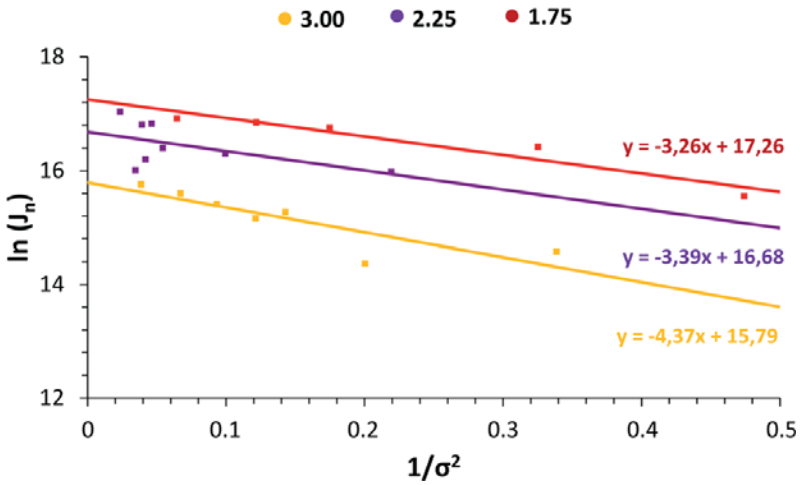

Fig. 4 Nucleation rates *versus* supersaturation. The logarithms of the determined nucleation rates are plotted against the inverse square of the supersaturation for gold nanorods with aspect ratios of 3.00 (yellow), 2.25 (purple), and 1.75 (red). The nucleation rates correlate with the aspect ratio of the gold nanorods.

With Ω being the volume per building unit of the solid phase, f being a numerical factor depending on the geometry of the nucleus, k_B being the Boltzmann constant, T being the temperature, A being a complicated function of the molecular-level parameters,[57] and E_A being the effective activation barrier. The calculated interfacial energies are summarized in ESI Table S3.† Herein, the interfacial energies increased with the decreasing gold nanorod aspect ratio. Furthermore, the nucleation barriers ΔG for the heterogeneous nucleation of gold nanorod-based superstructures on sulfonate-functionalized mica were calculated according to eqn (2).[5]

$$\Delta G = f\alpha^3 \left(\frac{V_M}{k_B T \sigma} \right)^2 \tag{2}$$

Fig. 5 shows the nucleation barriers obtained for different gold nanorod supersaturations. In general, the obtained nucleation barriers were low compared to the thermal energy, thereby favouring nucleation without a thermodynamic barrier at $\sigma > 2$ for all analysed aspect ratios. This result is not surprising if the opposite charges of particles and substrates are considered. Furthermore, the nucleation barriers augmented with increasing aspect ratio: gold nanorods with an aspect ratio of 3.00 exhibited the highest nucleation barriers (1.09 k_BT for $\sigma = 2$), while those of 2.25 and 1.75 hardly differed in terms of their magnitude (0.85 k_BT and 0.82 k_BT, respectively for $\sigma = 2$).

Finally, the kinetic and thermodynamic terms for the heterogeneous nucleation of the investigated gold nanorod superstructures were calculated (Table 1). The thermodynamic term constitutes the first addend in eqn (1) and the kinetic term constitutes the second addend. A low correlation was observed between the magnitude of the kinetic term and the nanorod anisotropy. For instance, the kinetic term increased when lowering the aspect ratios, indicating a decrease of E_A consistent with the higher nucleation rates depicted in Fig. 3. However, the obtained values hardly differ and are of the same magnitude. In general, the kinetic terms dominate over the thermodynamic ones. The magnitude of the thermodynamic term related to the nucleation barrier depends on the supersaturation σ and we determined the values for a supersaturation of 1.0 and two typical

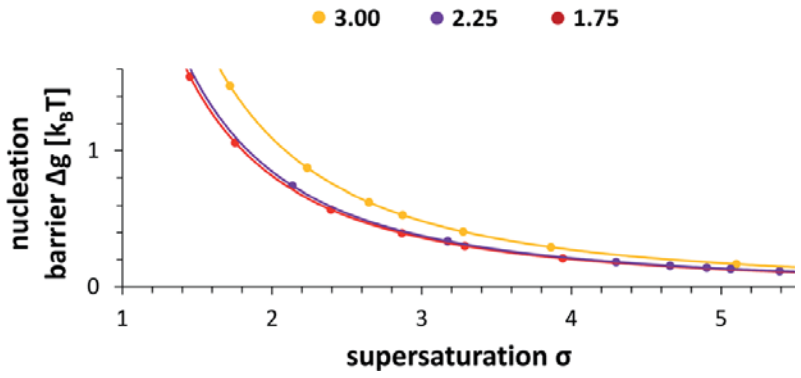

Fig. 5 Nucleation barrier. The nucleation barrier determined for the heterogeneous nucleation of gold nanorods is plotted against the supersaturation. The gold nanorods differ in their aspect ratio: 3.00 (yellow), 2.25 (purple), and 1.75 (red). The particles with the highest aspect ratio exhibit the highest nucleation barrier (3 : 1), while the nucleation barriers for the other two aspect ratios hardly differ.

Table 1 Kinetic and thermodynamic terms. The kinetic and thermodynamic terms determined for the heterogeneous nucleation of gold nanorod-based superstructures on sulfonate-functionalized mica substrates. Since the thermodynamic term is dependent on the supersaturation σ, we determined it for supersaturations of 1.0, 1.5, and 2.0

	3.00	2.25	1.75
Kinetic term	15.79	16.68	17.26
Thermodynamic term with $\sigma =$ 1.0	−4.37	−3.39	−3.26
Thermodynamic term with $\sigma =$ 1.5	−1.94	−1.51	−1.45
Thermodynamic term with $\sigma =$ 2.0	−1.09	−0.85	−0.82

Table 2 Growth conditions for gold nanorod synthesis

Localized surface plasmon resonance [nm]	Volume of silver nitrate 0.01 M solution [ml]	Volume of hydrochloric acid 1 M solution [ml]	Volume of small gold nanorod solution [μl]
630	0.4	—	50
730	2.0	2.0	50
800	2.5	6.0	40

supersaturations from our experiments: 1.5 and 2.0 (Table 1). The thermodynamic terms decrease in absolute numbers with decreasing aspect ratio indicating a decreasing nucleation barrier, which makes nucleation with a high aspect ratio thermodynamically less favourable than nucleation with a low aspect ratio. This finding is similar to the decreasing E_A with decreasing aspect ratio reflected in increasing kinetic terms. The values of the kinetic terms are dominating even for the lowest supersaturation of 1.0. This order of magnitude of thermodynamic and kinetic terms stands in contrast to typical molecular or ionic systems, for example, the nucleation of calcium carbonate on organothiol self-assembled monolayers.[5] As a rough estimate from the published graph, these examined systems showed thermodynamic terms of about −550, for a supersaturation σ of 1.0, which are significantly larger than the kinetic terms of around 40. The difference between the nanoparticle systems to ionic and molecular systems could be explained by a higher impact of diffusion for the nucleation with larger nanoparticles compared to small ions or molecules. This impact would make diffusion a crucial aspect for the heterogeneous nucleation of nanoparticle building units due to the more limited supply of building units to the nucleation site as compared to fast diffusing small ions or atoms. The increasing kinetic term with decreasing aspect ratios could support this idea (Table 1). Furthermore, a stronger diffusion is observed for the rods with a lower aspect ratio compared to those with a larger aspect ratio, due to the larger hydrodynamic radii of the latter. As the dominating kinetic term for the nucleation of gold nanorod-based superstructures stands in great contrast to the usually analysed atomic or molecular systems, further studies with nanoparticle systems would be of interest to verify whether this applies to the nucleation of nanoparticle building units in general.

Conclusions

It was possible to quantitatively investigate the heterogeneous nucleation phenomenon of superstructures based on anisotropic nanoparticles using a set of gold nanorods with different aspect ratios as a model system. Time-resolved light microscopy and UV-vis-NIR spectroscopy allowed for the determination of nucleation rates as well as the nanoparticle concentration in solution at each time. The UV-vis-NIR spectra allowed for a quantitative evaluation of the nucleation process by showing the time-dependent aggregation of the nanorods *via* spectral shifts of the nanorod longitudinal plasmonic band to longer wavelengths.

The shape of nanoparticles was found to strongly influence the heterogeneous nucleation rate of superstructures from anisotropic building blocks, as faster nucleation was noticed for nanorods with lower aspect ratios. In addition, evaluation of the nucleation rates in dependence of the supersaturation revealed a much larger kinetic nucleation barrier than the thermodynamic one. This is the opposite of the situation reported for the nucleation of ionic crystals like calcium carbonate.[5] The reason might be the much faster diffusion of ions than the nanorods and, therefore, a larger kinetic hindrance for the nucleation of the nanorod building units. On the other hand, the thermodynamic barrier did not practically exist for the investigated nanorods, as it was found to be $<1\ k_BT$ already for supersaturations >2, and only reached a few k_BT at its maximum at supersaturations approaching 1. The reason could be the electrostatic attraction between the negatively charged mica substrates and the positively charged nanorods, which almost eliminates the thermodynamic barrier, while the kinetic one is still significant.

Overall, our data set on heterogeneous nucleation of monodisperse nanorods with different anisotropy degrees into superstructures, provides important insight into the formation of superstructures from anisotropic nanoparticles. Moreover, the reported experiments can also serve as experimental data for theoretical descriptions of nucleation using non-spherical building units. The herein presented first results are limited, but a more systematic future investigation using the established experimental methodology can potentially yield larger data sets to systematically reveal the influence of the building unit shape on nucleation processes.

That a theory describing nucleation with anisotropic building units is important can already be seen from the fact that molecules are rarely spherical and also many particles are anisotropic. Therefore, understanding their nucleation and crystallization better could be truly beneficial for several applications ranging from nanoparticle superstructures like mesocrystals *via* macromolecular crystals in protein crystallization to the crystallization of small molecules in pharmaceuticals.

Experimental

Materials

All the starting materials were obtained from commercial suppliers and used without further purification: hexadecyltrimethylammonium bromide (CTAB, ≥99%), 1-decanol (*n*-decanol, 98%), hydrogen tetrachloroaurate trihydrate ($HAuCl_4 \cdot 3H_2O$, ≥99.9%), silver nitrate ($AgNO_3$, ≥99.0%), hydroquinone

(≥99.0%), L-ascorbic acid (≥99%), sodium borohydride ($NaBH_4$, 99%), *N*,*N*-diisopropylethylamine, and 3-aminopropyltriethoxysilane were purchased from Aldrich. Heptadecafluoro-1,1,2,2-tetrahydrodecyltriethoxysilane was purchased from ABCR. Ethanol (EtOH, ≥ 99.8%) and hydrochloric acid (HCl, 37.0%) were purchased from VWR. Nitric acid (HNO_3, ≥ 65%) was purchased from Carl Roth. MilliQ grade water (resistivity 18.2 MΩ cm at 25 °C) was used in all experiments. Mica sheets were obtained from micro to nano in different shapes with a thickness of 0.15 to 0.21 mm and the highest grade V-1 quality. Quartz cuvettes from VWR were used.

Synthetic procedures

Gold nanorods were synthesized according to a recently reported procedure.[47]

Synthesis of 1–2 nm gold seeds. 200 μl of a 0.05 M chloroauric acid solution and 200 μl of a 0.1 M ascorbic acid solution were added to 20 ml of a 50 mM CTAB and 13.5 mM *n*-decanol solution (prepared by dissolving 9.111 g of CTAB and 1.068 g in a 500 ml glass beaker in 500 ml of warm water, ∼60 °C, under stirring until complete dissolution). After 1–2 min, 800 μl of a freshly prepared 0.02 M sodium borohydride solution was injected under vigorous stirring (1000 rpm using a polytetrafluorethylene plain magnetic stirring bar: 30 × 6 mm) at 25–27 °C. The seed solution was aged for 30–60 min at room temperature prior to use.

Synthesis of small gold nanorods (21 nm in length and 7.5 nm in width). In a typical synthesis, 2400 μl of 0.01 M silver nitrate, 21 ml of 1 M hydrochloric acid, 3000 μl of 0.05 M chloroauric acid, and 3900 μl of 0.1 M ascorbic acid were added to 300 ml of a 50 mM CTAB and 11 mM *n*-decanol solution at exactly 25 °C (prepared by following the same procedure described for the 1–2 nm gold seeds). The growth was initiated by adding 18 ml of the seed solution under stirring. The mixture was left undisturbed at exactly 25 °C for at least 4 h. The obtained small gold nanorods, with a localized surface plasmon resonance longitudinal band located between 725–730 nm, were centrifuged at 14 000–15 000 rpm for 45–60 min in 2 ml tubes. The precipitate was redispersed with 4 ml of a 10 mM CTAB solution. The concentrated gold nanorods were centrifuged twice under the same conditions, and the final Au^0 concentration was fixed to 4.65 mM (Abs 400 nm: 1, optical path: 0.1 cm).

Synthesis of gold nanorods with distinct dimensions. In a typical synthesis, a certain amount of a 0.01 M silver nitrate solution (Table 2), 1 ml of 0.05 M chloroauric acid, 0.8 ml of a 0.1 M ascorbic acid solution (for nanorods with localized surface plasmon resonances at 730 nm and 800 nm), or 5 ml of a 0.1 M hydroquinone solution (for gold nanorods with localized surface plasmon resonances at 630 nm) were added under stirring, to 100 ml of a 50 mM CTAB and 11 mM *n*-decanol (for gold nanorods with localized surface plasmon resonances at 730 nm and 800 nm) solution or a 50 mM CTAB and 5.5 mM *n*-decanol (for gold nanorods with localized surface plasmon resonances at 630 nm) solution at 28 °C (Table 2). A certain volume of 1 M hydrochloric acid was subsequently added under stirring, and the growth was initiated *via* the addition of a given amount of small gold nanorod solution (Table 2). The mixture was left undisturbed for 4 h, and the obtained overgrown nanorods were washed by precipitation at 4000 rpm for 10 min and redispersed in 5 ml of a 1 mM CTAB solution.

Functionalization of mica substrates. Mica substrates were freshly cleaved using cello tape and treated with an oxygen plasma for 10 min at 80 W to generate

free hydroxyl groups. The surface functionalization was adapted from Crampton *et al.* and was carried out using a vapour phase diffusion under a protective gas atmosphere.[58] A 4 L desiccator was two times evacuated and flooded with nitrogen. The substrates were placed in the desiccator, followed by evacuation and flooding with nitrogen for a third time to reach a humidity under 25%. 60 µl of 3-aminopropyltriethoxysilane and 20 µl of 1,1-diisopropylethylamine were added to the desiccator in separate beakers. The desiccator was evacuated for 30 s, sealed afterwards and left for 2 h at RT. Afterwards, the functionalized substrates were baked for 2 h at 150 °C under ambient conditions to ensure the homogeneous distribution of the siloxanes on the surface and a complete crosslinking of the siloxane network. For functionalization with polystyrene sulfonate, the 3-aminopropyltriethoxysilane functionalized substrates were given into a solution of 1 wt% polystyrene sulfonate in water for 1 h. Afterwards, the surfaces were cleaned thoroughly with water and dried at 50 °C. All functionalized substrates were used in a period of one to two days after the functionalization.

Hydrophobisation of quartz cuvettes. The quartz cuvettes were cleaned in aqua regia for 1 h and afterwards cleaned thoroughly with water and treated with an oxygen plasma for 10 min at 80 W. The coating of quartz cuvettes with (heptadecafluoro-1,1,2,2-tetrahydrodecyl)methyldichlorosilane was performed similarly to the functionalization of mica substrates with 3-aminopropyltriethoxysilane except for the coating time, which amounted to 12 h instead of 2 h.

Nucleation experiments

Preparation of gold nanorod dispersions. The concentrated gold nanorods from the synthesis were washed with a 2 mM CTAB aqueous solution, centrifuged at 6000 rpm for 20 min, and the supernatant was removed. The washing procedure was repeated two times. A solution of 0.02 mM CTAB in water was prepared. The concentrated gold nanorods were added to the CTAB solution to reach the desired optical density. Before using the dispersion of gold nanorods in experiments, the stability of the gold nanorods was checked with UV-vis-NIR spectroscopy.

Destabilisation of gold nanorod dispersions. To destabilize the dispersion of gold nanorods, ethanol was added to an amount of 20 vol% (for the microscopic analysis). During or after the destabilization experiments, the formed aggregates and remaining single particles were stabilized again using an excess amount of CTAB. This allowed freezing and analysing aliquots at their actual destabilization stage. Therefore, a CTAB solution was added to adjust the amount of CTAB to 2.00 mM. To analyse the structures formed on mica surfaces, the mica platelets were washed thoroughly with water and dried with a nitrogen stream at RT.

Image analysis. During the experiments, light microscope pictures were taken every 30 s and processed with ImageJ respective to Fiji. A Trainable Weka Segmentation was applied, differentiating between nuclei on the surface, background and moving aggregates in solution. The classifier results were given out as results and the number of nuclei species was counted. Therefore, a threshold (MaxEntropy) was applied and the number of nuclei was counted using the analyse particles function (size = 10 − infinity pixel). The number of counted species of the first picture (only background, structure growth did not start yet) was subtracted from all following results.

Determination of supersaturation. For the determination of the gold nanorod concentrations, the optical density at 400 nm was taken from UV-vis-NIR spectra. After Hendel *et al.*, we assumed an extinction coefficient of 2.685 l mol^{-1} cm for our gold nanorods.[59] With the Beer–Lambert law (eqn (3)) the Au(0) concentration c was calculated since we knew the extinction E_λ from the UV-vis-NIR measurements and the depth of the used cuvette d.[60]

$$E_\lambda = \varepsilon_\lambda c d \tag{3}$$

With this, the Au(0) concentration of the solution was known. However, in the system, the monomer was not the gold atom but the gold nanorods. Therefore, the gold nanorod concentration had to be calculated from the Au(0) concentration. The volume for each gold nanorod aspect ratio was calculated: 6.02×10^{-22} m^3 (3.00), 4.52×10^{-22} m^3 (2.25), and 3.52×10^{-22} m^3 (1.75). Gold only forms a face-centred cubic package with a lattice parameter of 0.4078 nm resulting in the volume of the unit cell of 0.07 nm^3.[61] With this, the number of gold unit cells fitting into one gold nanorod was calculated. One gold unit cell contains 4 atoms of gold which gave us the number of gold atoms in one gold nanorod: 3.56×10^7 (3.00), 2.67×10^7 (2.25), and 2.08×10^7 (1.75).[62] With this quantity, we converted the Au(0) concentration into a gold nanorod concentration.

To calculate the supersaturation σ, the concentration of gold nanorods in a saturated solution x^* was determined for each particle surface system. Therefore the Au(0) concentration after the destabilization of the nanorods (when a steady state was reached) was determined with UV-vis-NIR spectroscopy and the corresponding gold nanorod concentration was calculated. Finally, the resulting supersaturation for each destabilization experiment at a gold nanorod concentration x was calculated with eqn (4).

$$\sigma = \frac{x}{x^*} \tag{4}$$

Instruments

HR-TEM images were recorded on a JEOL JEM-2200FS microscope at an accelerating voltage of 200 kV. The samples were applied on Quantifoil carbon-coated Cu 400 mesh grids.

Light microscopy images were recorded with an AxioImager from Zeiss with an LD Epiplan 50×/0.50 HD DIC objective using transmitted light, bright field illumination, a condenser numerical aperture at 0.9, an Axiocam 506 bw as an imaging device, and an exposure time of 10 ms.

SEM images were recorded with a Gemini500 by Zeiss operating at 3 kV equipped with an Inlens and a secondary electron detector for secondary and backscattered electrons. Samples were coated with a 2.5 nm platinum layer, mounted on aluminium stubs, and attached by carbon conductive layers.

UV-vis-NIR measurements were performed with a Varian Cary 50 spectrometer in quartz cuvettes. The UV-vis-NIR measurements carried out simultaneously with light microscopy measurements were performed with a modular USB2000+ spectrometer from Ocean Optics equipped with a USB-DT miniature deuterium tungsten halogen lamp.

Author contributions

A. G. performed the investigation, formal analysis, methodology, visualization and project administration for this project. G. G.-R. provided resources (gold nanorods) and conceptualized this project. H. C. secured the funding, conceptualized and administrated this project. All authors contributed to writing of this manuscript.

Conflicts of interest

There are no conflicts to declare.

Acknowledgements

This work was supported by the Deutsche Forschungsgemeinschaft (SFB 1214, Project B3). G. G.-R. gratefully acknowledges the Alexander von Humboldt Foundation for financial support. We thank the BIC of the University of Konstanz for providing the light microscope instrumentation and assistance with the imaging and analysis of the pictures. Furthermore, we thank the PAC and the Nano Lab of the University of Konstanz for providing the SEM and TEM.

Notes and references

1 D. W. Oxtoby, *J. Phys.: Condens. Matter*, 1992, **4**, 7627.
2 J. J. De Yoreo and P. G. Vekilov, *Rev. Mineral. Geochem.*, 2003, **54**, 57–93.
3 K. Sangwal, *Nucleation and Crystal Growth: Metastability of Solutions and Melts*, 2018.
4 S. A. Walling and J. L. Provis, *Chem. Rev.*, 2016, **116**, 4170–4204.
5 M. H. Nielsen, J. R. I. Lee, Q. N. Hu, T. Y. J. Han and J. J. De Yoreo, *Faraday Discuss.*, 2012, **159**, 105–121.
6 R. P. Sear, *J. Phys.: Condens. Matter*, 2007, **19**, 033101.
7 L. Assoud, F. Ebert, P. Keim, R. Messina, G. Maret and H. Löwen, *J. Phys.: Condens. Matter*, 2009, **21**, 464114.
8 H. J. Schöpe and T. Palberg, *J. Phys.: Condens. Matter*, 2002, **14**, 11573.
9 V. de Villeneuve, D. Verboekend, R. Dullens, D. Aarts, W. Kegel and H. Lekkerkerker, *J. Phys.: Condens. Matter*, 2005, **17**, S3371.
10 S. Auer and D. Frenkel, in *Advanced Computer Simulation*, Springer, 2005, pp. 149–208.
11 B. J. Alder and T. E. Wainwright, *J. Chem. Phys.*, 1957, **27**, 1208–1209.
12 W. W. Wood and J. D. Jacobson, *J. Chem. Phys.*, 1957, **27**, 1207–1208.
13 P. N. Pusey and W. Van Megen, *Nature*, 1986, **320**, 340–342.
14 L. Antl, J. Goodwin, R. Hill, R. H. Ottewill, S. Owens, S. Papworth and J. Waters, *Colloids Surf.*, 1986, **17**, 67–78.
15 S.-E. Phan, W. B. Russel, Z. Cheng, J. Zhu, P. M. Chaikin, J. H. Dunsmuir and R. H. Ottewill, *Phys. Rev. E: Stat., Nonlinear, Soft Matter Phys.*, 1996, **54**, 6633–6645.
16 R. S. Jardine and P. Bartlett, *Colloids Surf., A*, 2002, **211**, 127–132.
17 U. Gasser, *J. Phys.: Condens. Matter*, 2009, **21**, 203101.
18 J. R. Savage and A. D. Dinsmore, *Phys. Rev. Lett.*, 2009, **102**, 198302.

19 A. Nonat, *Cem. Concr. Res.*, 2004, **34**, 1521–1528.
20 P. Nadeau, *Clay Miner.*, 1985, **20**, 499–514.
21 I. Soroka, in *Portland Cement Paste and Concrete*, Springer, 1979, pp. 28–45.
22 J. Holcomb, N. Spellmon, Y. Zhang, M. Doughan, C. Li and Z. Yang, *AIMS Biophys.*, 2017, **4**, 557–575.
23 C. Lizandara-Pueyo, S. Siroky, M. R. Wagner, A. Hoffmann, J. S. Reparaz, M. Lehmann and S. Polarz, *Adv. Funct. Mater.*, 2011, **21**, 295–304.
24 Y. Kang, M. Li, Y. Cai, M. Cargnello, R. E. Diaz, T. R. Gordon, N. L. Wieder, R. R. Adzic, R. J. Gorte and E. A. Stach, *J. Am. Chem. Soc.*, 2013, **135**, 2741–2747.
25 M. Aslam, R. Bhobe, N. Alem, S. Donthu and V. Dravid, *J. Appl. Phys.*, 2005, **98**, 074311.
26 M. Darques, L. Piraux and A. Encinas, *Appl. Phys. Lett.*, 2005, **86**, 072508–072511.
27 S. Polarz, *Adv. Funct. Mater.*, 2011, **21**, 3214–3230.
28 E. V. Sturm and H. Cölfen, *Chem. Soc. Rev.*, 2016, **45**, 5821–5833.
29 D. V. Talapin, *MRS Bull.*, 2012, **37**, 63.
30 Z. W. Quan and J. Y. Fang, *Nano Today*, 2010, **5**, 390–411.
31 S. Y. Zhang, M. D. Regulacio and M. Y. Han, *Chem. Soc. Rev.*, 2014, **43**, 2301–2323.
32 H. Cölfen and M. Antonietti, *Mesocrystals and Nonclassical Crystallization*, John Wiley & Sons, 2008.
33 H. Cölfen and M. Antonietti, *Angew. Chem., Int. Ed.*, 2005, **44**, 5576–5591.
34 M. Niederberger and H. Cölfen, *Phys. Chem. Chem. Phys.*, 2006, **8**, 3271–3287.
35 M. A. Boles, M. Engel and D. V. Talapin, *Chem. Rev.*, 2016, **116**, 11220–11289.
36 W. D. Luedtke and U. Landman, *J. Phys. Chem.*, 1996, **100**, 13323–13329.
37 L. Jiang, X. D. Chen, N. Lu and L. F. Chi, *Acc. Chem. Res.*, 2014, **47**, 3009–3017.
38 Y. Zhou, X. Z. Zhou, D. J. Park, K. Torabi, K. A. Brown, M. R. Jones, C. Zhang, G. C. Schatz and C. A. Mirkin, *Nano Lett.*, 2014, **14**, 2157–2161.
39 Y. Cui, M. T. Bjork, J. A. Liddle, C. Sonnichsen, B. Boussert and A. P. Alivisatos, *Nano Lett.*, 2004, **4**, 1093–1098.
40 C. Hanske, E. H. Hill, D. Vila-Liarte, G. González-Rubio, C. Matricardi, A. Mihi and L. M. Liz-Marzán, *ACS Appl. Mater. Interfaces*, 2019, **11**, 11763–11771.
41 X. Wang, J. Feng, Y. Bai, Q. Zhang and Y. Yin, *Chem. Rev.*, 2016, **116**, 10983–11060.
42 A. D. Dinsmore, M. F. Hsu, M. G. Nikolaides, M. Marquez, A. R. Bausch and D. A. Weitz, *Science*, 2002, **298**, 1006–1009.
43 Y. Lin, A. Boker, H. Skaff, D. Cookson, A. D. Dinsmore, T. Emrick and T. P. Russell, *Langmuir*, 2005, **21**, 191–194.
44 J. He, Q. Zhang, S. Gupta, T. Emrick, T. R. Russell and P. Thiyagarajan, *Small*, 2007, **3**, 1214–1217.
45 Y. Xia, K. D. Gilroy, H. C. Peng and X. Xia, *Angew. Chem., Int. Ed.*, 2017, **56**, 60–95.
46 M. N. O'Brien, M. R. Jones, K. A. Brown and C. A. Mirkin, *J. Am. Chem. Soc.*, 2014, **136**, 7603–7606.
47 G. Gonzalez-Rubio, V. Kumar, P. Llombart, P. Diaz-Nunez, E. Bladt, T. Altantzis, S. Bals, O. Pena-Rodriguez, E. G. Noya, L. G. MacDowell, A. Guerrero-Martinez and L. M. Liz-Marzan, *ACS Nano*, 2019, **13**, 4424–4435.
48 M. Grzelczak, J. Vermant, E. M. Furst and L. M. Liz-Marzán, *ACS Nano*, 2010, **4**, 3591–3605.

49 J. Liao, Y. Zhang, W. Yu, L. Xu, C. Ge, J. Liu and N. Gu, *Colloids Surf., A*, 2003, **223**, 177–183.
50 V. Myroshnychenko, J. Rodríguez-Fernández, I. Pastoriza-Santos, A. M. Funston, C. Novo, P. Mulvaney, L. M. Liz-Marzán and F. J. G. De Abajo, *Chem. Soc. Rev.*, 2008, **37**, 1792–1805.
51 L. M. Liz-Marzán, *Langmuir*, 2006, **22**, 32–41.
52 G. Haran and L. Chuntonov, *Chem. Rev.*, 2018, **118**, 5539–5580.
53 R. Yu, L. M. Liz-Marzán and F. J. G. de Abajo, *Chem. Soc. Rev.*, 2017, **46**, 6710–6724.
54 G. González-Rubio, J. González-Izquierdo, L. Bañares, G. Tardajos, A. Rivera, T. Altantzis, S. Bals, O. Peña-Rodríguez, A. Guerrero-Martínez and L. M. Liz-Marzán, *Nano Lett.*, 2015, **15**, 8282–8288.
55 D. J. Schupp, J. Angst, E. A. Schaefer, S. M. Schupp and H. Cölfen, *J. Phys. Chem. C*, 2021, **125**, 20343–20350.
56 A.-K. Göppert, G. González-Rubio and H. Cölfen, *J. Phys. Chem. A*, 2020, 5657–5663.
57 O. Galkin and P. G. Vekilov, *J. Phys. Chem. B*, 1999, **103**, 10965–10971.
58 N. Crampton, W. A. Bonass, J. Kirkham and N. H. Thomson, *Langmuir*, 2005, **21**, 7884–7891.
59 T. Hendel, M. Wuithschick, F. Kettemann, A. Birnbaum, K. Rademann and J. r. Polte, *Anal. Chem.*, 2014, **86**, 11115–11124.
60 A. Beer, *Ann. Phys.*, 1852, **162**, 78–88.
61 F. M. Mirabella, *Internal reflection spectroscopy: theory and applications*, CRC Press, 1992.
62 F. M. Fowkes, *Ind. Eng. Chem. Res.*, 1964, **56**, 40–52.